AIAA Propulsion and Energy Forum
August 9-11, 2021, VIRTUAL EVENT
AIAA Propulsion and Energy 2021 Forum

10.2514/6.2021-3703

Analysis and Reconstruction of Zefiro 40 Solid Rocket Motor Static Firing Tests and Extrapolation to Flight

Daniele Bianchi*, Marco Grossi†, Bernardo Favini‡,
Sapienza University of Rome, Rome, Italy§
Ferruccio Serraglia¶, Nicola Ierardo‖,
*ESA ESRIN, Frascati, Italy***

An independent assessment of the steady-state and tail-off ballistic performance of the two static firing tests of Zefiro 40 solid rocket motor has been performed. The analysis is carried out with a post-firing 0D quasi-steady performance reconstruction model, developed for the purpose and already used for the analysis of VEGA SRM SFTs. The study has been focused on two different aspects: i) the SFTs ballistic performance analysis with the reconstruction of the non-ideal parameters and the performance extrapolation to flight configuration; ii) the motor performance extrapolation to flight unit based on the reconstructed non-ideal parameters and exploiting the SFT to flight expertise of Zefiro 23 SRM. The final goal is to increase the understanding of VEGA's solid rocket motors behavior in terms of non-ideal parameters and to consolidate the methodology used for the performance reconstruction and extrapolation to flight unit.

Nomenclature

$\dot{m}$	=	mass flow rate, $\mathtt{kg/s}$
$\dot{m}_{\text{eros}}$	=	ablation mass flux, $\mathtt{kg/m^2 \cdot s}$
η_{c^*}	=	combustion efficiency
η_{c_F}	=	thrust efficiency
$\hat{p}$	=	experimental head-end pressure, $\mathtt{N/m^2}$
$\hat{T}$	=	experimental thrust, $\mathtt{N}$
ρ_p	=	solid propellant density, $\mathtt{kg/m^3}$
a	=	temperature coefficient, $\mathtt{m/s}$
A_t	=	nozzle throat area, $\mathtt{m^2}$
c^*	=	characteristic velocity, $\mathtt{m/s}$
c_F	=	thrust coefficient
h	=	hump parameter
M_p	=	loaded propellant mass, $\mathtt{kg}$
n	=	combustion index
p	=	chamber pressure, $\mathtt{N/m^2}$
r_b	=	propellant burning rate, $\mathtt{m/s}$
S_b	=	burning surface, $\mathtt{m^2}$

*Ph.D., Associate Professor, Member AIAA, e-mail: daniele.bianchi@uniroma1.it
†Ph.D. student, e-mail: marco.grossi@uniroma1.it
‡Associate Professor, e-mail: bernardo.favini@uniroma1.it
§Dipartimento di Ingegneria Meccanica e Aerospaziale, Via Eudossiana 18, Roma 00184, Italy.
¶Ph.D., VEGA/P120C Senior Solid Propulsion Engineer STS-DC and STS-DVL, Member AIAA, e-mail: ferruccio.serraglia@esa.int
‖Ph.D., VEGA Launcher Stages Engineering Manager ESA-ESRIN/STS-DVL, Member AIAA, e-mail: nicola.ierardo@esa.int
**VEGA Integrated Project Team, Via Galileo Galilei, 00044 Frascati (Rome), Italy.

SF = scale factor
T = thrust, N
t = time, s
t_b = burning time, s
T_i = propellant initial temperature, K
web = web thickness, m

Subscripts

id = ideal
ref = reference

I. Introduction

The ability to accurately predict, reconstruct and extrapolate internal ballistics and performance, in terms of specific and total impulse, of a solid rocket motor prior to static firing and test flight of the motor itself is of paramount importance due to the effect that analysis results can have on motor design and development.[1–7] In this work, the internal ballistics and performance reconstruction analysis of high performance solid rocket motors (SRMs) is carried out with a 0D quasi-steady model that is based upon an inverse and a direct approach. The inverse approach, on the one hand, relies on the static firing test measurements in order to evaluate the behavior of the motor, through the reconstruction of the non-ideal parameters: combustion efficiency, thrust efficiency, hump curve, scale factor and nozzle throat area evolution. The direct approach, on the other hand, uses the non-ideal parameters reconstructed by the inverse approach to extrapolate the motor performance in flight. The final goal is to increase the understanding of solid rocket motors behavior in terms of non-ideal parameters in order to assess the overall motor performance, to enrich the knowledge of the motor behavior, to characterize motor dispersion and scattering, and to consolidate the methodology used for the performance reconstruction and extrapolation to flight unit (FU).

The selected case study for the model analysis and verification is the Zefiro 40 solid rocket motor, the second stage propulsion system of the Vega C launch system, whose demonstration and qualification static firing tests took place in 2018 and 2019, respectively. Avio is responsible for the development and qualification of the Zefiro 40 solid rocket motor.[8–10] Avio development of the Zefiro 40 began in 2011, with the goal of overcoming the intrinsic limits of the Zefiro 23, the current second stage propulsion system of the Vega launcher. As compared with its predecessor Zefiro 23, in fact, Zefiro 40 has a higher average pressure, increased propellant mass fraction, improved structural design margins for the casing and propellant grain, and a flexible joint with low resistant torque. Zefiro 40 is loaded with about 36 metric tons of HTPB composite propellant. The length is comparable with that of Zefiro 23 one as well as the throat area, while the diameter has been incrased to 2.4 m. The final goal is that of increasing SRM overall performance and reliability as well as cost competitiveness.

II. Solid Rocket Motor performance reconstruction model

The post-firing reconstruction model is able to assess, in the SRM quasi-steady state and tail-off phase, the actual behavior of the SRM during the firing through the evaluation of the non-ideal parameters and the nozzle throat area evolution in time based on a functional dependence of nozzle throat erosion from motor operating conditions.[6,7,11–14] The non-ideal parameters take into account the SRM actual behavior with respect to: i) the propellant burning rate, typically coming from small-scale single grain batch tests for propellant characterization (BARIA), and the uncertainties on the full-scale propellant grain burning surface evolution, which are taken into account through the product of the hump and scale factor;[15] ii) the shift of the propellant combustion products thermochemical characterization with respect to the ideal equilibrium adiabatic conditions,[16] considered in the combustion efficiency; iii) the thrust efficiency to characterize all the thrust losses in the nozzle expansion process, i.e. divergence, two-phase flow, boundary-layer losses and frozen flow effects. These parameters are evaluated exploiting the experimental measures occurring before, during and after the static firing test, and the reconstruction technique, along with its main assumptions and modeling parameters. The data measured before and during the static firing test regarding the motor internal ballistics are typically the following: the loaded propellant mass (from the experimental measures); the initial and final nozzle throat area value and the nozzle expansion ratio (from quality and post-firing measurements);

the propellant density (from the experimental measures); the head-end pressure (from the experimental measures); the measured or reconstructed SRM thrust (from the test bench data); the propellant burning rate characterization in terms of a and n parameters of the de Saint-Robert-Vieille law (evaluated by small-scale BARIA propellant grain batch analyses). Finally, the nominal evolution of the combustion surface in the web is theoretically evaluated by grain burn-back analysis.

The burning rate model for the quasi-steady phase is the classical de Saint-Robert-Vieille law

$$r_b(t) = a(T_i) \left(\frac{p(t)}{p_{ref}} \right)^n \tag{1}$$

where any significant effect related to dynamic burning during both the ignition transient and the tail-off phases and/or erosive burning effects have been neglected.[17,18]

Then, the characteristic velocity is defined by Eq. (2).

$$c^*(t) = \frac{p(t)\ A_t(t)}{\dot{m}(t)} \tag{2}$$

Also the thrust coefficient is the classical expression given in Eq. (3).

$$c_F(t) = \frac{F(t)}{p(t)\ A_t(t)} \tag{3}$$

The combustion products thermochemical characterization (in terms of their average molecular mass and specific heat ratio) along with the adiabatic flame temperature and the ideal characteristic velocity, c^*_{id}, are evaluated by means of the CEA[16] chemical equilibrium code assuming equilibrium and adiabatic combustion (ideal case). The ideal thrust coefficient, $c_{F_{id}}$, is calculated by means of ideal nozzle theory and propellant thermochemical characterization. The nominal evolution of the burning surface in the web thickness is theoretically evaluated by grain burn-back analysis,[17–19] assuming a spatially constant burning rate in accordance with the 0D model.

For the throat erosion and the throat diameter evolution during the firing of the flight units, as no direct measure of the final nozzle throat can be performed, post-firing correlations extracted from the static firing tests of each motor and a more general functional law derived from numerical analyses and propellant thermochemical characterization can used. The semi-empirical correlations gathered from SFTs expertise[5,6] and/or the functional law obtained from numerical analyses[13] represent a thermochemical characterization in terms of nozzle throat ablation mass flux dependency upon motor chamber pressure.

The overall performance reconstruction problem can be expressed in terms of the non-ideal parameters: combustion efficiency η_{c^*}, hump, scale factor, and thrust efficiency η_{c_F}, to be determined as follows.

The combustion efficiency is exploited in order to ensure the overall mass balance during the firing, given the total loaded propellant mass, M_p, the experimental pressure-time evolution, $\hat{p}(t)$, and the ideal characteristic velocity, $c^*_{id}(t)$:

$$\eta_{c^*} = \frac{\displaystyle\int_0^{t_b} \frac{\hat{p}(t) A_t(t)}{c^*_{id}(t)} dt}{M_p} \tag{4}$$

where the ideal characteristic velocity, $c^*_{id}(t)$, is a function of both the propellant thermochemical characterization and of the experimental pressure-time evolution, $\hat{p}(t)$.

The product of the hump parameter, h, and the scale factor, SF, can be evaluated for each time instant, assuming the use of a 0D quasi-steady model, through the instantaneous mass balance inside the combustion chamber, as given by Eq. (5).

$$SF \cdot h(web(t)) = \frac{\dfrac{\hat{p}(t) A_t(t)}{\eta_{c^*} c^*_{id}(t)}}{\rho_p\ S_b(web(t))\ a(T_i) \left(\dfrac{\hat{p}(t)}{p_{ref}} \right)^n} \tag{5}$$

For the characterization of the thrust efficiency, η_{c_F}, the thrust-time evolution, $\hat{F}(t)$, as well as the ambient pressure variation (if any) during the burning time are assumed as input:

$$\eta_{c_F}(t) = \frac{\hat{F}(t)}{\frac{\hat{p}(t)\ A_t(t)}{c_{F_{id}}(t)}} \tag{6}$$

where the ideal thrust coefficient, $c_{F_{id}}(t)$, is a function of the propellant thermochemical characterization (through the exhaust gases specific heat ratio), the nozzle area ratio (that depends upon the throat erosion process), and the chamber to ambient pressure ratio (that depends on the experimental pressure-time evolution, $\hat{p}(t)$, and on the experimental ambient pressure variation, $\hat{p}_a(t)$).

In order to perform the analysis, the following input data are considered for the motor:

- the measured head-end pressure inside the motor as a function of time;
- the measured/reconstructed thrust produced by the motor as a function of time;
- the measured atmospheric pressure variation (if any) as a function of time;
- the propellant burning rate characteristics coming from the BARIA tests;
- the total propellant mass loaded, the igniter propellant mass, the thermal protection & liner ejected mass, the nozzle & igniter thermal protection ejected mass, and the alumina slag (if any) deposition mass;
- the solid propellant thermochemical characterization and the theoretical properties of its combustion products;
- the burning surface evolution over the web of the propellant grain;
- the density of the nozzle throat insert thermal protection.

As far as the nozzle expansion ratio of the motor is concerned, for upper stage SRMs that are designed to operate in vacuum, the SFT motor nozzle is characterized by a reduced (cut-off) nozzle expansion ratio as it is operated in atmospheric conditions. Moreover, in terms of propellant formulation, some differences are also present among the flight unit (FU) and demonstration (DM) and qualification (QM) motors, in terms of additives and particles granulometry, in order to obtain the desired propellant characteristics in terms of ballistic parameters and combustion. In order to perform the ballistic performance reconstruction, the measured head-end pressure inside the chamber as a function of time and the measured thrust-time evolution during the burn are to be considered as input data for the model. From the post-firing expertise of the SFT the final throat diameter is also measured, although its evolution in time is not known a priori. Therefore, to perform the ballistic reconstruction of the SFT and the performance extrapolation of the flight unit motor, a characterization in terms of nozzle throat erosion rate dependence upon the motor operational conditions is required. A characterization in terms of nozzle throat ablation dependency upon motor operational conditions was derived in Ref. [13]. The erosion rate-time evolution is reconstructed from the pressure-time trace of the motor, a functional law of the type $\dot{m}_{\text{eros}} = bp_c^m$ (named BPM), and the known density of the thermal protection material. By integrating the erosion rate-time evolution one obtains the nozzle throat erosion and hence the throat diameter- and the throat area-time evolution. It has to be considered that the erosion rate build-up is typically characterized by a short time delay (of the order of a few seconds, depending on several factors) during which the throat erosion rate is only a fraction of its steady-state value. Hence, the throat area-time evolution can be reconstructed assuming different erosion time delays during which it is assumed that the erosion rate builds up.

The selected case study for the model analysis and verification is the Zefiro 40 solid rocket motor, whose DM and QM static firing tests took place at the rocket testing range of Salto di Quirra, Sardinia, on March 2018 and on May 2019, respectively. Zefiro 40 motor,[8–10] developed and manufactured by Avio in their Colleferro factory, is the second stage propulsion system of the Vega C orbital launch system, an evolution of the current Vega launcher, that is scheduled to lift off for its maiden flight in 2021. This work provides a summary of the activities related to the critical review and the independent assessment of the ballistic performance of Zefiro 40 SRM. The main goal of this work is to reconstruct the actual performance of the DM and QM motors and to provide an assessment of the non-ideal parameters characterizing the actual SRM behavior in terms of: i) the hump curve and the scale factor; ii) the combustion efficiency; iii) the thrust

efficiency; and iv) the nozzle throat area evolution. The second objective is to perform the performance extrapolation to the flight unit in order to assess the thrust curve and the specific impulse of the flight unit SRM. The analysis is organized into two main parts: 1) the Zefiro 40 DM and QM static firing tests ballistic performance analysis with the reconstruction of the non-ideal parameters and the performance extrapolation to flight configuration using an inverse approach; and 2) the motor performance extrapolation to flight unit using a direct approach based on the previously reconstructed non-ideal parameters and exploiting the SFT to flight expertise of Zefiro 23 SRM.

For confidentiality reasons, in the following analysis, all the sensible data of the Zefiro 40 motor are provided in non-dimensional form.

III. Propellant thermochemical characterization

In order to perform the ballistic performance reconstruction, the solid propellant thermochemical characterization and the theoretical properties of its combustion products in terms of specific heat ratio, molecular weight, flame temperature, and characteristic velocity and their variation with the operational conditions is required. The Zefiro 40 HTPB2013 propellant is presented in Table 1. This is an 86.85/20 (percentage of solids/percentage of aluminum) hydroxyl-terminated polybutadiene binder (HTPB) propellant with a formation enthalpy of -1778.05 kJ/kg at standard temperature conditions, i.e. 298.15 K. Thermochemical analyses are performed with the NASA Chemical Equilibrium with Applications (CEA) code.[16] Figures 1(a) to 2 show the exhaust gas properties vs pressure from chemical equilibrium calculations assuming adiabatic combustion and isentropic expansion. Mixture properties that varies because of the expansion process, such as mixture specific heat ratio and molecular weight, are evaluated at two locations: the combustion chamber and the nozzle throat.

Table 1. Zefiro 40 HTPB2013 propellant formulation

Component	**Mass Fraction**, %
Ammonium Perchlorate	66.85
Aluminum	20.00
HTPB	9.33
additives	3.82

Figure 1 shows the exhaust gas mixture thermodynamic and performance properties as a function of motor chamber pressure compared with the corresponding reference data provided by Avio. The agreement between the calculated and the reference value for the specific heat ratio at the reference pressure is very good, provided that a reduced dataset including 16 chemical species is used (as listed in Fig. 1(a)). Differences between values calculated in the chamber or at the throat are rather marginal for the reduced dataset and, furthermore, the reference data is closely confined within the two values. The agreement between the calculated and the reference value for the molecular weight at the reference pressure is good (see Fig. 1(b)), and the reference data is confined within the values obtained from the full and from the reduced datasets. Differences between values calculated in the chamber or at the throat are, on the other hand, negligibly small. The agreement between the calculated and the reference value for the flame temperature at the reference pressure is very good (see Fig. 1(c)), and the reference data is closely confined within the values obtained from the full and from the reduced datasets. Finally, the agreement between the calculated and the reference value for the ideal characteristic velocity at the reference pressure is very good (see Fig. 1(d)), provided that the values of both mixture specific heat ratio and molecular weight at the throat location are used to compute the ideal characteristic velocity. Differences between values calculated from the full and from the reduced datasets are rather marginal. Overall, the approach that is providing the best agreement with the reference data is that of using the reduced dataset with mixture values evaluated at the throat location. Evaluating the gas properties at the throat location is a reasonable assumption, considering that a single location has to be assumed for the entire motor (including the nozzle and its divergent part) within a zero-dimensional internal ballistics approach. The use of a reduced dataset, including only the most dominant exhaust gases, with respect to a complete data set that is comprising more than 300 species, is justified by the lack of information

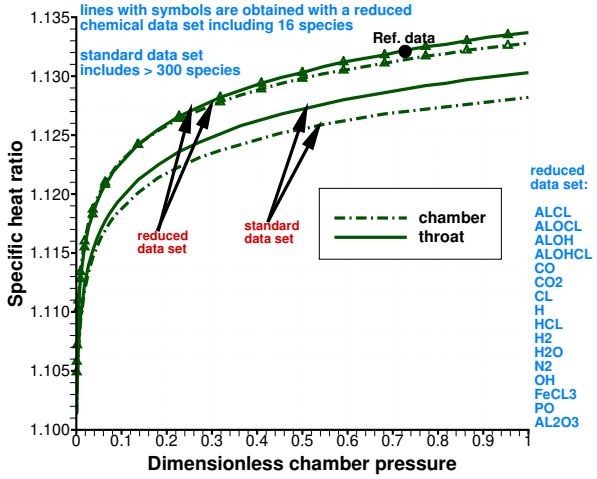

(a) Mixture specific heat ratio vs pressure

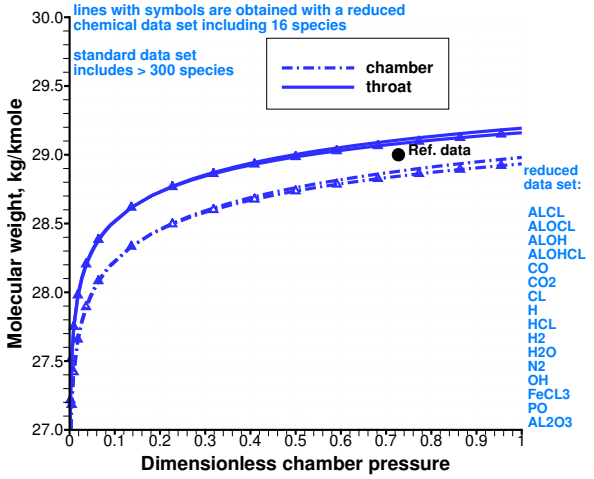

(b) Mixture molecular weight vs pressure

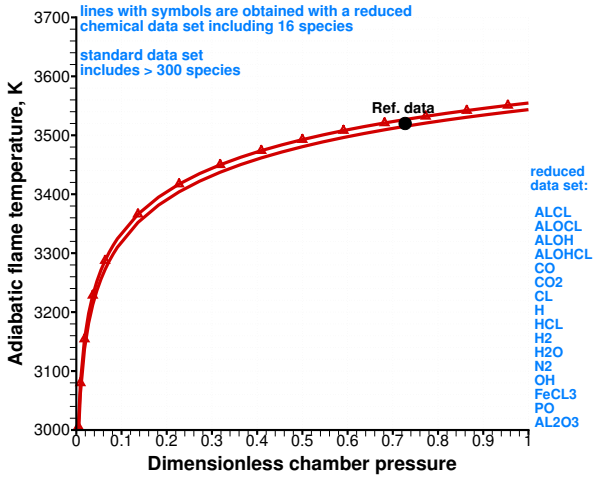

(c) Adiabatic flame temperature vs pressure

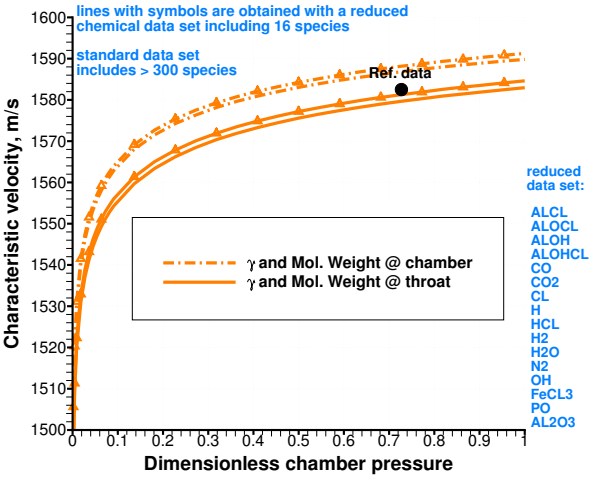

(d) Ideal characteristic velocity vs pressure

Figure 1. Propellant properties vs pressure from chemical equilibrium calculations with different assumptions (black dot is the reference data).

about the substantial amount of species that could potentially be present in the exhaust gases. Experience, insight, and experimental data are all important ingredients in the development of accurate thermochemical datasets for a selected solid propellant formulations. In addition, to illustrate the energy content of the propellant, Fig. 2 shows the propellant specific thermal energy as a function of motor chamber pressure. The specific thermal energy is evaluated as the difference between the formation enthalpy of the exhaust gases mixture and the formation enthalpy of the solid propellant at standard temperature conditions. The result is a specific thermal energy in between 5.5 MJ/kg at the minimum operational pressure and 5.9 MJ/kg at the maximum operational pressure. With a total propellant mass of ≈ 36 metric tons and a burning time of ≈ 100 s, this corresponds to a thermal energy output of ≈ 2.1 GW for the motor.

In order to be fully consistent with the reference data, the computed results have been calibrated according to the reference values at the corresponding reference pressure. In conclusion, as the differences between propellant theoretical properties evaluated from chemical equilibrium calculations (using the reduced dataset with mixture values evaluated at the throat location) and the corresponding reference data is either null or negligibly small at the reference pressure after a slight calibration, it can be reasonably assumed that

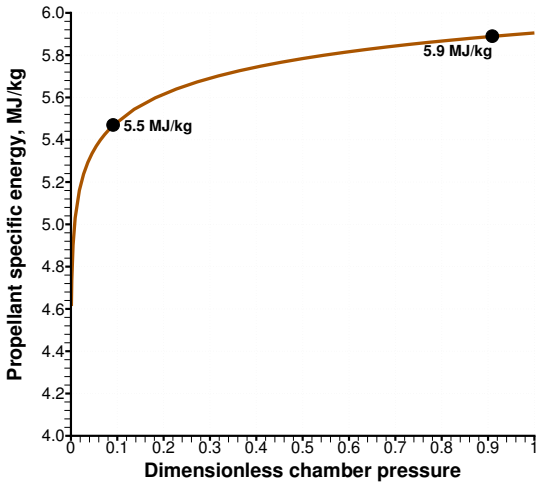

Figure 2. Propellant specific thermal energy vs pressure from chemical equilibrium calculations.

the whole propellant thermochemical characterization as a function of pressure is also consistent with the reference data. Hence, the Zefiro 40 HTPB2013 propellant can be considered fully characterized in terms of thermochemical behavior.

IV. Ballistic performance analysis

The Zefiro 40 SRM internal ballistic analysis has been performed for both the DM and the QM unit, using different assumptions for the throat diameter-time evolution and for the propellant thermochemical properties variation with combustion efficiency.

IV.A. Motor performance analysis of steady-state & tail-off

Zefiro 40 DM and QM tests took place at Salto di Quirra, Sardinia, on March 7th 2018 and on May 7th 2019, respectively. The recorded ambient pressure was 1.01 bar for DM and 1.02 bar for QM. The recorded SRM internal pressure was 1.34 bar for DM and 1.33 bar for QM. The recorded propellant mean bulk temperature was 18.8 °C for DM and 19.8 °C for QM. In order to perform the ballistic performance reconstruction of the steady-state & tail-off phases, the measured forward chamber pressure-time evolution inside the combustion chamber and the measured axial thrust-time evolution during the burn are to be considered as input data for the model.

Figure 3 shows the analysis forward chamber pressure and its derivative vs time as retrieved from the two high pressure transducers placed in the combustion chamber for both QM and DM SFTs. The two redundant transducers showed a very good agreement during all motor functioning for both DM and QM. Measures difference are well inside the transducers accuracy (±0.34 bar), except for a very limited time window at the burnout for QM, hence no correction was required. The maximum operating pressure, the time at maximum pressure, and the burning time are perfectly reproduced with respect to the reference data. The resulting pressure integral of the retrieved pressure-time curve matches perfectly with the reference data from Avio, with a percentage difference of less than 0.05% for both DM and QM. Figure 4(a) shows a comparison of the forward chamber pressure measured from DM and QM SFTs. The pressure integral of QM SFT is roughly 0.5% lower with respect to DM SFT. Figure 4(b) shows the analysis axial thrust at sea level vs time retrieved from the axial bench thrust cells (A and B bridges for redundancy) for both QM and DM SFTs. There are four axial bench thrust cells for each bridge. The two bridges A and B showed very good agreement during all motor functioning for both QM and DM. Measures difference among bridge A and B are well inside the thrust cell accuracy (1125 N for a load from 0 to 750 kN, linearly increasing up to 2250 N for a load from 750 to 1500 kN, i.e. 100% capacity), hence no correction was required for both DM and QM. The resulting thrust integral of the retrieved axial thrust-time curve matches perfectly with the reference data, with a

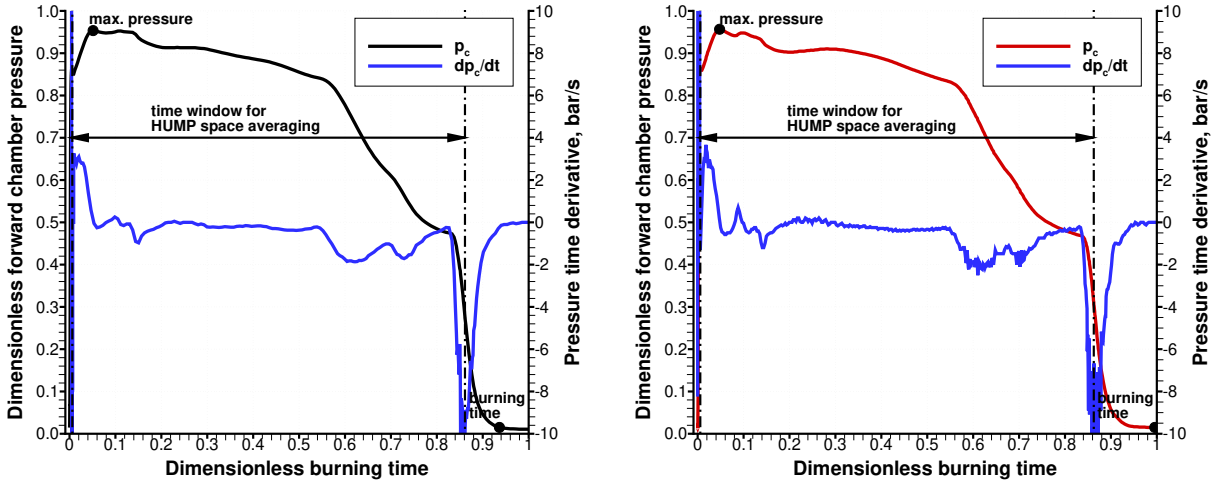

(a) DM static firing test.

(b) QM static firing test.

Figure 3. Forward chamber pressure and its derivative vs time during steady-state & tail-off.

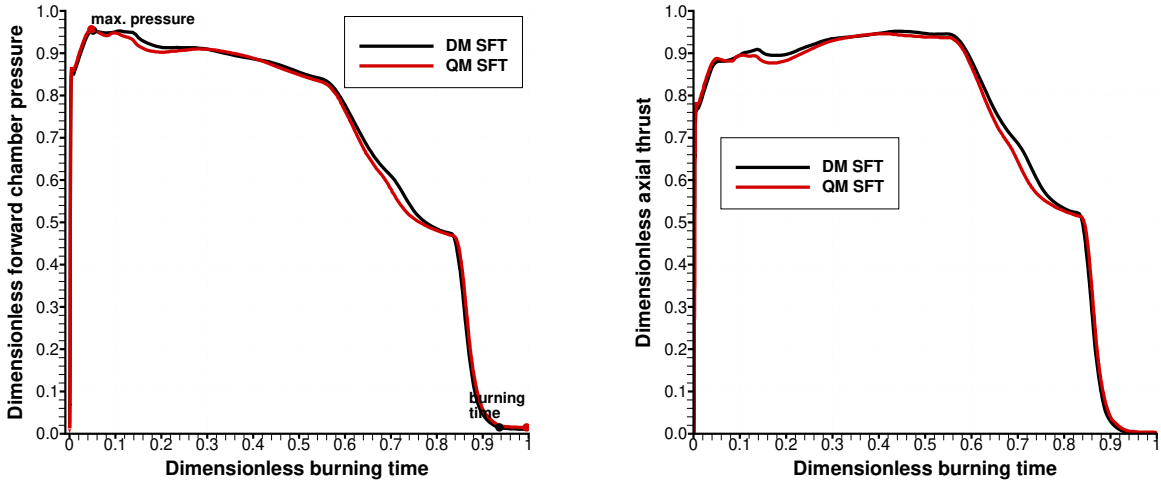

(a) Forward chamber pressure vs time.

(b) Axial thrust at sea level vs time.

Figure 4. Motor performance during steady-state & tail-off for both DM and QM SFTs.

percentage difference of less than 0.05% for both DM and QM. The thrust integral of QM SFT is roughly 1% lower with respect to DM SFT.

IV.B. Loaded and ejected masses

In order to perform the ballistic performance reconstruction of the steady-state & tail-off phases, the total propellant mass loaded, the igniter propellant mass, the thermal protection & liner ejected mass, the nozzle & igniter thermal protection ejected mass, and the alumina slag (if any) deposition mass are required.

Table 2 lists all of the above mentioned masses for the Zefiro 40 DM and QM motors. In particular, it is worth noting that the ratio of ejected inerts over ejected propellant is equal to roughly 0.6% for DM and 0.4% for QM. The ratio of ejected inerts over ejected propellant is relevant for the combustion efficiency evaluation, as inerts contribution to the motor chamber pressure has to be assessed.

Table 2. Zefiro 40 DM and QM motor masses (all masses are in kilograms)

Motor	DM SFT	QM SFT
Propellant loaded	36110	36120
Propellant igniter	9	9
Total propellant	36119	36129
Alumina slug	19	20
Total ejected propellant	36100	36109
Total ejected inerts	224	149
Total ejected mass	36324	36258

IV.C. Burning surface characterization

In order to perform the ballistic performance reconstruction of the steady-state & tail-off phases, the burning surface evolution of the propellant grain is required. The burning surface evolution as a function of the web thickness was derived via DIMA tools. Firstly, the initial shape of the propellant grain has been reconstructed by using GRAD (GRAin Design) tool. Secondly, the geometry created by GRAD is evolved from ignition through burnout by using GREG (Grain REGression) tool.[19] Results of the combined use of GRAD and GREG tools is schematically shown in Fig. 5. The burning surface evolution at different non dimensional web thickness (w_a) is also reported in Fig. 5, showing the propellant grain viewed from both the outside and the inside. As for all aft-finocyl SRMs, the star shaped region is almost completely burnt out in the early phase of motor operational life.

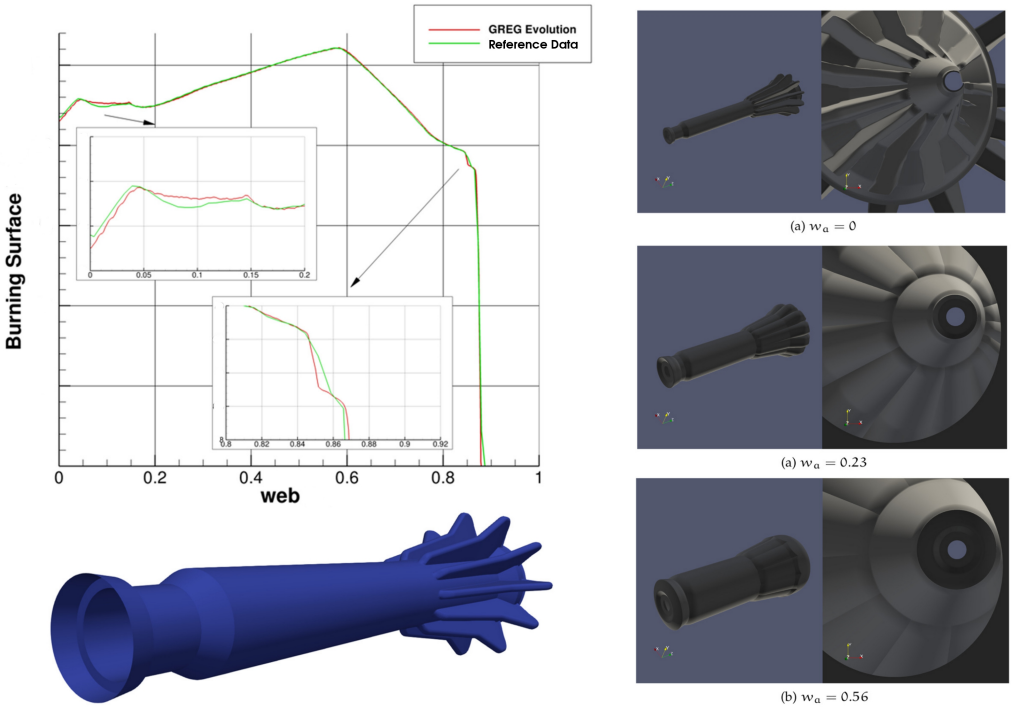

Figure 5. Schematic of burning surface reconstruction (via GRAD tool) and burning surface evolution (via GREG tool).

Figure 6 shows a comparison of the burning surface evolution over the web thickness reconstructed from GRAD + GREG tools with respect to the reference burning surface evolution from Avio. As shown, the two curves show a very good agreement, with a percentage difference that is mostly confined within ±0.3% throughout the whole web thickness. Maximum differences (±0.8%) are located in two narrow regions near

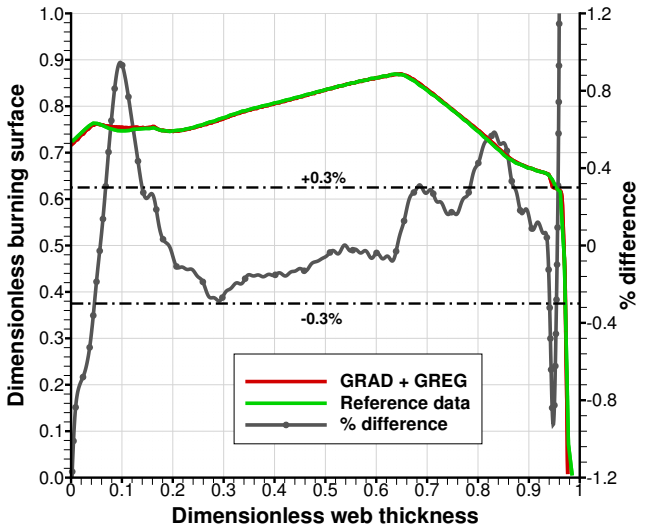

Figure 6. Burning surface evolution as a function of web thickness: GRAD + GREG result vs reference data.

dimensionless web 0.1 and near dimensionless web 0.85. Overall, differences in the burning surface evolution over the web are relatively small. Hence, in the following analyses, only the burning surface evolution from reconstructed data from GRAD + GREG will be adopted.

IV.D. Nozzle throat erosion characterization

In order to perform the ballistic performance reconstruction of the steady-state & tail-off phases, the nozzle throat erosion characterization is required. A characterization in terms of nozzle ablation dependency upon motor operational conditions was derived via a CFD analysis in the framework of a previous activity. In particular, a characterization in terms of throat ablation mass flux dependency upon motor chamber pressure was derived for the Zefiro 40 carbon-carbon nozzle insert and the HTPB2013 propellant thermochemical characterization through a power-fitting of the numerical data performed at discrete chamber pressure levels.

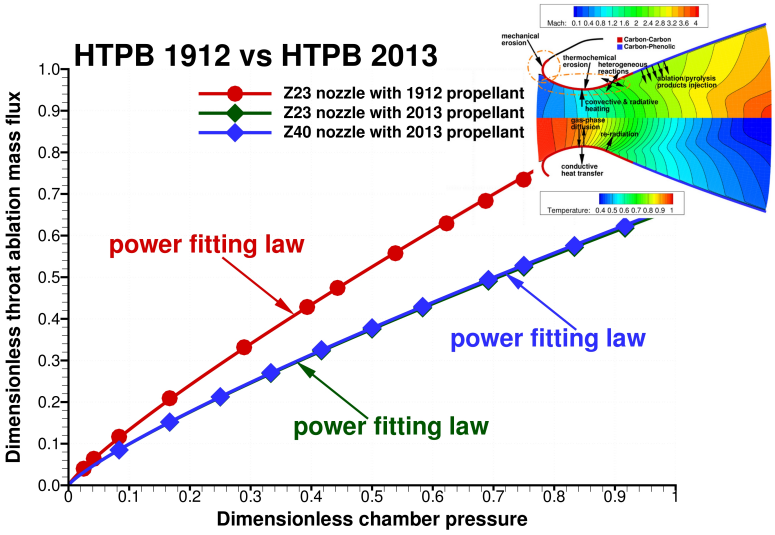

Figure 7. Zefiro 23 and Zefiro 40 nozzle throat erosion characterization from CFD simulations for HTPB1912 and HTPB2013 propellant with BPM ($\dot{m}_{\mathrm{eros}} = bp_c^n$) power regression.

The results of such a functional law (named BPM) for the evolution of the throat area are reported in Fig. 7, including also results for HTPB1912 propellant and Zefiro 23 nozzle as a reference. As shown, the BPM law provides a throat ablation evolution that is functionally dependent on chamber pressure. It is worth noting that the throat ablation mass flux at Zefiro 40 reference chamber pressure is predicted to be −28% for HTPB2013 with respect to HTPB1912, while nozzle shape differences (Z40 vs Z23) play a very marginal role. Hence, from a thermochemical standpoint, the HTPB2013 appears to be significantly less oxidizing for the carbon-based throat insert material.

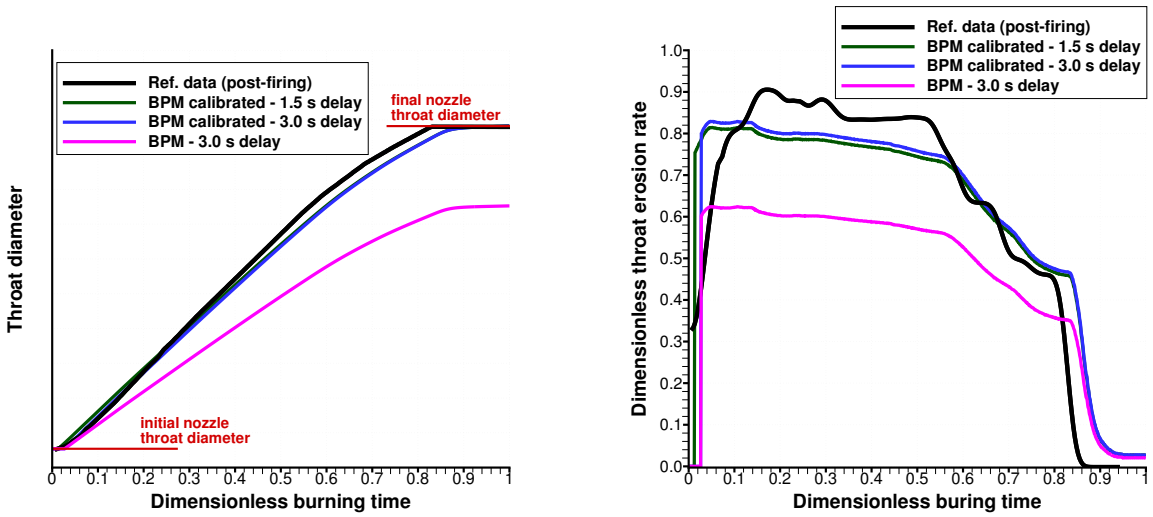

(a) Throat diameter-time evolution

(b) Throat erosion rate-time evolution

Figure 8. Zefiro 40 DM nozzle throat-time evolution: BPM and BPM calibrated (with different time delays) vs reference law (post-firing).

The erosion rate-time evolution is reconstructed from the pressure-time trace of the motor, the BPM functional law ($\dot{m}_{\text{eros}} = bp_c^m$), and the known density of the thermal protection material. By integrating the erosion rate-time evolution one obtains the nozzle throat erosion and hence the throat diameter- and the throat area-time evolution.

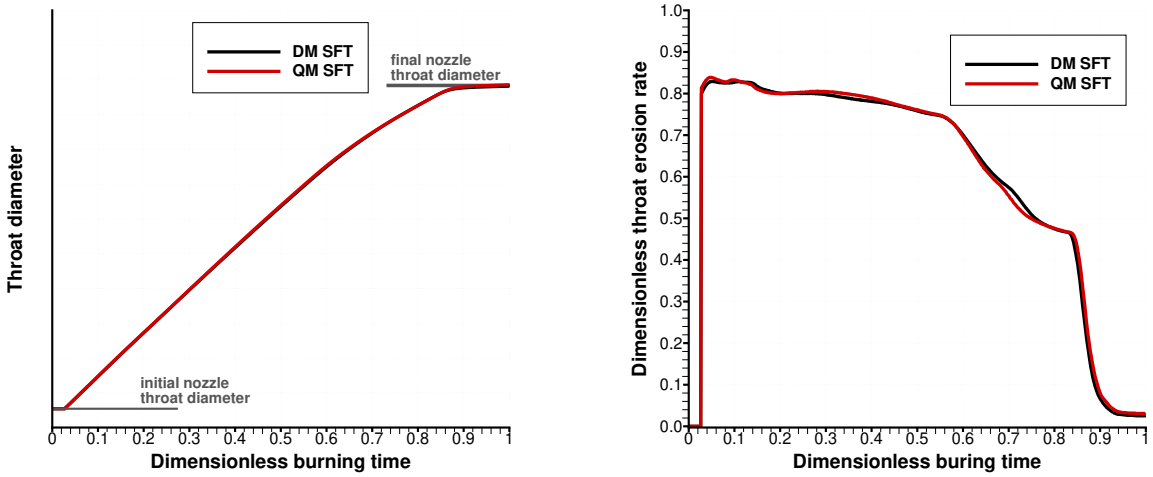

(a) Throat diameter-time evolution

(b) Throat erosion rate-time evolution

Figure 9. Zefiro 40 DM and QM nozzle throat-time evolution using BPM calibrated with 3.0 s delay.

It has to be considered that the erosion rate build-up is typically characterized by a short time delay

(of the order of a few seconds, depending on several factors) during which the throat erosion rate is only a fraction of its steady-state value. The throat area-time evolution can be reconstructed assuming different erosion time delays during which it is assumed that the erosion rate is simply zero, as shown in Fig. 8 for DM SFT assuming two time delays of 1.5 and 3 seconds, respectively. The BPM law with no calibration (assuming a reference C/C density) results in a final throat diameter erosion that is underestimated by 25% with respect to SFT post-firing expertise (see Fig. 8(a)). The possible causes for such an underestimation are many (propellant more chemically aggressive than theoretically predicted, possible contributions from mechanical erosion/spallation, missing material characterization, porosity, roughness, ...) and would definitely require more detailed data in terms of throat material characterization (whereas density was the only known parameter). Hence, exploiting the SFT post-firing expertise, the BPM has been calibrated in order to obtain a final throat prediction that matches the experimental data. The major difference between the BPM throat-time evolution and the reference law from Avio is mainly in the tailoff region where the reference law drops abruptly to zero erosion while the BPM is flatting out more gently as the pressure decays (see Fig. 8(b)).

Fig. 9 shows the Zefiro 40 DM and QM nozzle throat diameter- and erosion rate-time evolution using BPM calibrated with 3.0 s delay, which is assumed as the reference value for the following analyses. The effect of the nozzle throat erosion delay on the reconstructed non-ideal parameters and the performance extrapolation is extensively discussed in Ref. [7]. It is worth noting that DM and QM SFTs showed very consistent results in terms of nozzle erosion, with post-firing experimental measurements (used for calibration) showing less than 0.5% difference in the eroded thermal protection material thickness at the throat between the two motors (see Fig. 9(a)).

V. Assessment of the non-ideal parameters

As described in the previous section, the results of the static firing reconstruction have been obtained considering the calibrated BPM correlation with 3.0 s delay for the nozzle throat erosion, as shown in Fig. 9.

V.A. Hump and scale factor reconstruction

Figure 10(a) shows the total hump (i.e. hump x SF) curves obtained for the two static firings. As discussed in Ref. [7], the erosion law as well as the nozzle throat erosion delay have a marginal effect on the total hump curve. Hence, both the hump and the scale factor can be considered to be substantially independent from the adopted throat erosion law.

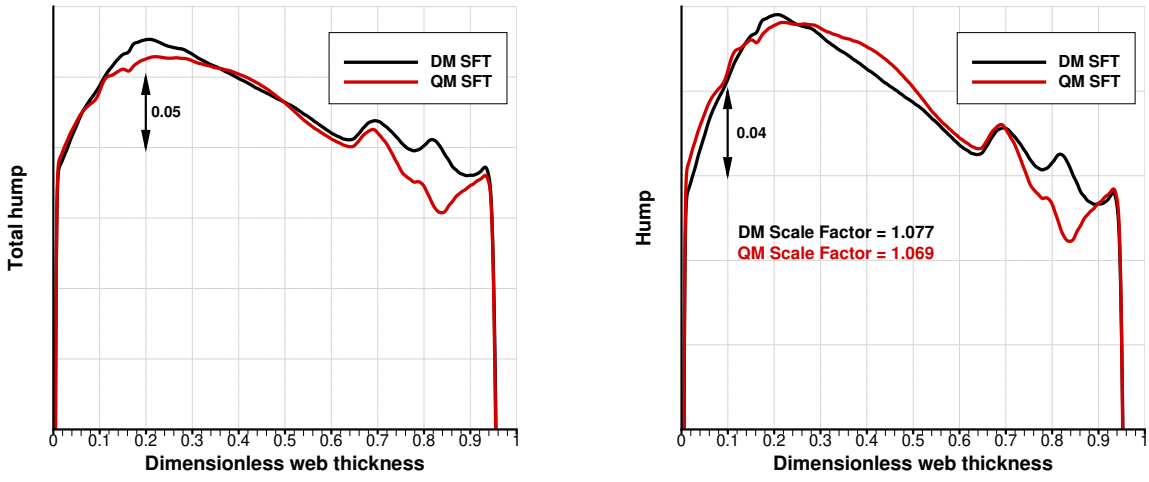

(a) Total hump. (b) Hump.

Figure 10. Zefiro 40 hump predictions for both DM and QM SFTs.

Figure 10(b) shows the obtained results in terms of hump curve. It is worth noting the presence of a

typical peak in the hump curve at approximately 0.2 in dimensionless web thickness for both SFTs, although peak web is not clearly evident for QM as it is for DM. The hump strongly decays at approximately 0.95 in dimensionless web thickness for both SFTs. The scale factor obtained from analysis (regardless of erosion law) is 1.077 for DM and 1.069 for QM. Hence, a reduction of approximately 10% (from 7.7% down to 6.9%) in the scale factor is experienced from DM to QM. This reduction was expected as a possible consequence due to an anomaly experienced in the ammonium perchlorate granulometry distribution for QM (coarser product with respect to DM one). Finally, DM and QM reconstructed experimental hump curves are globally similar except for the presence of an inverse oscillation for QM with respect to DM in the last part of the burn (i.e. close to thermal protection/liner wall of the cylindrical region), approximately from 0.7 to 0.9 dimensionless web thickness (see Fig. 10(b)). This could be linked to a different propellant particle size distribution during the casting process of QM wrt DM motor, again possibly related to the above mentioned oxidizer granulometry anomaly.

V.B. Combustion efficiency reconstruction

Table 3 lists the combustion efficiencies for Zefiro 40 DM and QM obtained using two different correlations for the nozzle throat erosion: i) BPM calibrated (with 3 s delay); and ii) reference post-firing erosion law from Avio. Results are computed excluding the ejected inerts from the calculation of the combustion efficiency. As previously discussed, that ejected inerts mass represent a small but non negligible fraction (of the order of 0.5% with respect to the ejected propellant mass), hence its treatment affects the combustion efficiency. One extreme is that of excluding the ejected inerts from the combustion efficiency calculation, i.e. assuming that they do not contribute at all in pressurizing the combustion chamber; the other extreme is that of including the ejected inerts in the combustion efficiency calculation, i.e. assuming that they do contribute in pressurizing the combustion chamber as if they were propellant. The latter assumption always results in a lower combustion efficiency prediction. However, this is not particularly relevant for motor performance extrapolation if predictions are done consistently, as long as the ejected inerts mass of the flight unit is expected to be comparable to the one from the SFTs.

Table 3. Zefiro 40 SFTs reconstructed combustion efficiency

SFT	**nozzle erosion law**	**c-star efficiency**, %
DM	BPM with 3.0 s delay	97.37
DM	reference law	98.03
QM	BPM with 3.0 s delay	96.76
QM	reference law	97.11

As shown in Tab. 3, the effect of a different nozzle throat erosion law on the reconstructed combustion efficiency is evident. It is worth noting that, excluding inerts from the calculation, the combustion efficiency using the reference post-firing erosion law is almost identical to the reference data (98.09% for DM and 97.17% for QM). Regardless of the throat erosion law used, the QM firing is characterized by a lower combustion efficiency with respect to DM one. Such a reduction is the major responsible for the reduced pressure integral of QM wrt DM (see Fig. 4(a)), despite a slightly higher propellant temperature coefficient (faster burning rate) for QM wrt DM. A possible explanation for this combustion efficiency reduction can be found in the previously mentioned anomaly experienced in the ammonium perchlorate granulometry distribution for QM. This anomaly, in fact, could lead to a different particle packing inside the solid propellant which in turn could cause a different (i.e. bigger) agglomerate size, which is typically associated with a reduction in combustion efficiency.

V.C. Thrust efficiency reconstruction

The ideal thrust coefficient is calculated by means of the ideal nozzle theory and the propellant thermochemical characterization (through the exhaust gases specific heat ratio). Figure 11 shows the thrust efficiency curves obtained including (γ_{var}) or excluding (γ_{fix}) specific heat ratio variations with combustion efficiency and using BPM calibrated (with 3 s delay). Note that the thrust efficiency is evaluated neglecting thrust

vectoring (as no data were available). When combustion efficiency effects are also extended to the mixture properties (such as specific heat ratio), a lower combustion efficiency value also translates into a lower specific heat ratio value, as shown in Fig. 12. Results in Fig. 12 have been obtained using two different correlations for the nozzle throat erosion for Z40 DM: i) BPM calibrated (with 3 s delay); and ii) reference post-firing erosion law from Avio. This also implies that, when specific heat ratio variations with combustion efficiency are included, the specific heat ratio and its time-evolution become also affected by the nozzle throat erosion law (see Fig. 12).

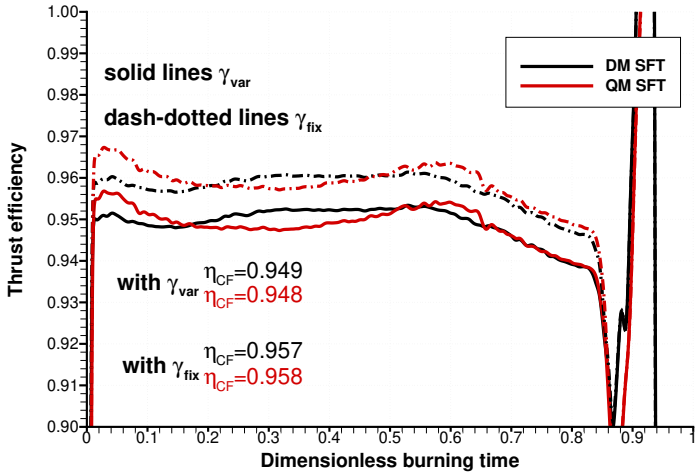

Figure 11. Zefiro 40 SFTs thrust efficiency curves with or w/o γ variation with combustion efficiency (average values are also shown).

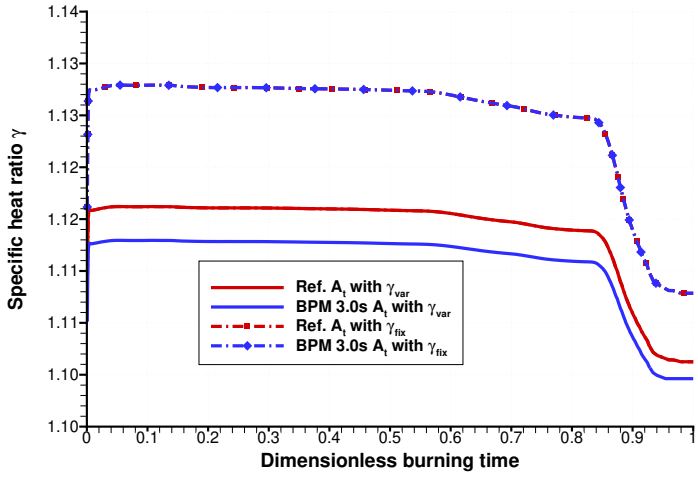

Figure 12. Zefiro 40 DM specific heat ratio variations for different throat erosion laws and with or w/o variation with combustion efficiency.

As shown in Fig. 11 the thrust efficiency is rather constant (although this is less true for QM) up to roughly mid-burn, and then it starts to decrease almost linearly with time. Moreover, the thrust efficiency tends to increase when excluding specific heat ratio variations with combustion efficiency (i.e. γ_{fix}) as the ideal thrust coefficient decreases with increasing specific heat ratio. An average thrust efficiency value (based on total impulse) can be derived from the thrust efficiency-time curve. Using the reference post-firing erosion law and the BPM calibrated law (with 3 s delay) the obtained average thrust efficiencies over the burning time are shown in Tab. 4. Results indicate that thrust efficiencies are very similar for DM and QM tests

when BPM calibrated is used. Differently, a slightly higher thrust efficiency is shown for QM with respect to DM when the reference post-firing erosion law from Avio is used.

Table 4. Zefiro 40 SFTs reconstructed combustion efficiency

SFT	nozzle erosion law	gamma, γ	thrust efficiency, %
DM	BPM with 3.0 s delay	variable	94.92
DM	BPM with 3.0 s delay	fixed	95.73
DM	reference law	variable	94.42
DM	reference law	fixed	95.05
QM	BPM with 3.0 s delay	variable	94.83
QM	BPM with 3.0 s delay	fixed	95.79
QM	reference law	variable	94.56
QM	reference law	fixed	95.43

Interestingly and not surprisingly, one should always expect higher thrust efficiencies for the nozzle throat erosion law that is producing lower combustion efficiencies and vice-versa, as the overall efficiency, $\eta_{C_F}(t)\cdot\eta_{c^*}$, shall remain (almost) constant unless the ideal thrust coefficient-time evolution is significantly affected. The overall efficiency obtained for DM SFT using BPM calibrated (with 3 s delay) and assuming variable specific heat ratio with combustion efficiency (i.e. γ_{var}) and excluding ejected inerts is $0.9492 \cdot 0.9737 = 0.9242$ while the one obtained using the reference post-firing erosion law and assuming variable specific heat ratio with combustion efficiency (i.e. γ_{var}) and excluding ejected inerts is $0.9442 \cdot 0.9803 = 0.9256$. Hence, almost identical overall efficiencies are obtained despite the different throat erosion laws adopted. Similar results are also obtained with QM SFT, with overall efficiencies of 0.9176 using BPM calibrated and of 0.9183 using the reference post-firing erosion law.

V.D. Performance extrapolation to flight configuration

In order to carry out the performance extrapolation to flight configuration (FC), the motor performance has to be assessed in vacuum condition and using the (higher) flight unit (FU) nozzle expansion ratio but using the same propellant ballistic parameters of the SFT motor (i.e. no change in the burning time).

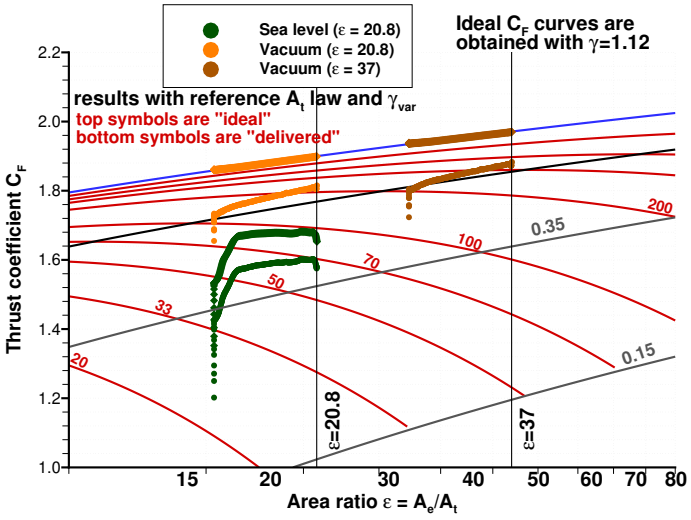

Figure 13. Zefiro 40 DM thrust efficiency evolution over nozzle area ratio for sea level and vacuum operations and different nozzle expansion ratios (20.8 for the SFT DM unit and 37 for the flight unit).

Figure 13 shows the ideal thrust coefficient as a function of the nozzle area ratio for Z40 DM. The ideal

thrust coefficient curves have been computed assuming a constant specific heat ratio γ of 1.12 (representative of the γ value in a wide pressure range of $\approx 50 - 100$ bar, see Fig. 12) and for different values (from 20 to 1000) of the chamber to ambient pressure ratio. The vacuum curve (chamber to ambient pressure ratio equal to infinity) is shown in blue. The plot is also indicating the initial value of the area ratio for Zefiro 40 nozzle. Two values have been assumed: i) the SFT value of 20.8 (reduced with respect to the flight unit because of the constraint derived from the nozzle operation at atmospheric pressure) and ii) the flight unit value of 37. Both ideal and delivered values for Zefiro 40 DM SRM are reported. Results have been obtained assuming the reference post-firing law for nozzle throat erosion and variable specific heat ratio with combustion efficiency (i.e. γ_{var}). The thrust efficiency in vacuum and for the higher expansion ratio of the flight unit is assumed to be the same as the one reconstructed from the SFT conditions (i.e. sea level and reduced nozzle expansion ratio). The validity of this assumption will be discussed in the next part (analysis of thrust efficiency increase from SFT to flight).

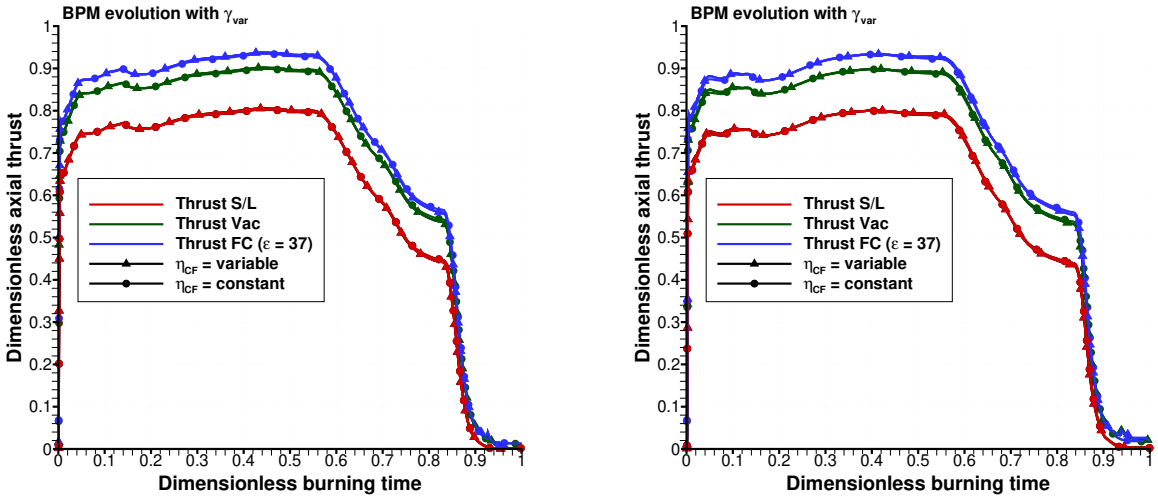

(a) DM motor (20.8 nozzle expansion ratio).

(b) QM motor (20.9 nozzle expansion ratio).

Figure 14. Zefiro 40 delivered thrust at sea level and vacuum operations for static firing test and flight unit nozzle expansion ratio (i.e. flight configuration) and assuming both time-variable and average thrust efficiency.

Figure 14 shows the Zefiro 40 delivered thrust at sea level and vacuum operations for two nozzle expansion ratios: i) 20.8 (DM) and 20.9 (QM) corresponding to the SFT unit, both sea level and vacuum; and ii) 37 corresponding to the flight unit (FU), vacuum only. Results have been obtained assuming the BPM calibrated law (with 3 s delay) for nozzle throat erosion and variable specific heat ratio with combustion efficiency (i.e. γ_{var}). Curves are obtained assuming the time-variable thrust efficiency (shown in Fig. 11) or a constant average value (based on total impulse). Results shows that the assumption of using a constant average value for the thrust efficiency is reasonable and produces negligible effects on the thrust-time evolution. Hence, the thrust-time evolution is negligibly affected by the $\eta_{C_F}(t)$ evolution over time as almost identical results are obtained if a constant η_{C_F} is adopted (this is useful for performance extrapolation to SRM flight unit).

The obtained delivered I_{sp} for DM motor, including the extrapolation to flight configuration (vacuum and FU nozzle), are as follows: i) 245.7 s for sea level operation and $\epsilon = 20.8$; ii) 280.3 s for vacuum operation and $\epsilon = 20.8$; and iii) 291.6 s for vacuum operation and $\epsilon = 37$ (FC).

The obtained delivered I_{sp} for QM motor, including the extrapolation to flight configuration (vacuum and FU nozzle), are as follows: i) 243.3 s for sea level operation and $\epsilon = 20.9$; ii) 279.2 s for vacuum operation and $\epsilon = 20.8$; and iii) 290.0 s for vacuum operation and $\epsilon = 37$ (FC).

It is worth noting that the above listed data are obtained assuming that the thrust efficiency in vacuum and for the higher expansion ratio of the flight unit is the same as the one reconstructed from the SFT conditions (reduced expansion ratio and atmospheric operation). Flight expertise demonstrates that this is not the case, as usually thrust efficiency increases from SFTs to flights.

VI. Analysis of thrust efficiency increase from SFT to flight

As far as the thrust efficiency comparison between flights and SFTs is concerned, the analysis of Zefiro 23 and Zefiro 9 motors is useful as it shows higher values of the thrust efficiency over time for the flights with respect to the static firings, especially for the Zefiro 9 motor. It is worth recalling that, as for Zefiro 40, the SFT and the FU nozzle configuration is not the same for the Zefiro 9 and Zefiro 23 motors, as the SFT nozzle is characterized by a reduced expansion ratio that is not optimized for atmospheric pressure operation (which may justify the lower thrust efficiency). Another difference is, obviously, in terms of the nozzle operational condition, as the SFTs are at constant ambient pressure (sea level) while the flights are in vacuum condition.

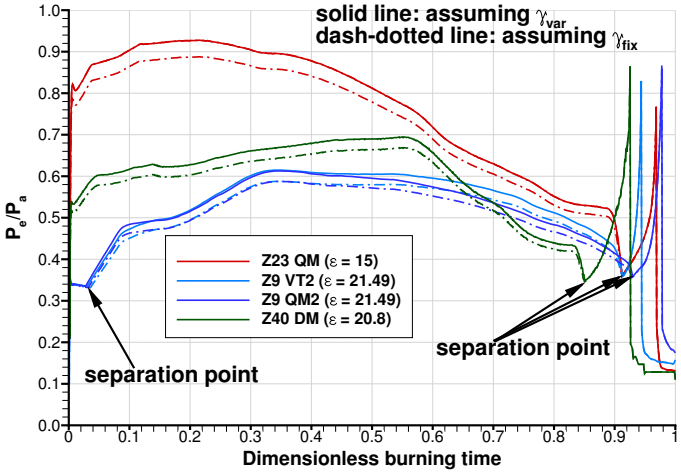

Figure 15. Comparison of nozzle over-expansion condition (in terms of p_e/p_a) for the SFTs of Zefiro 9 (QM2 and VT2), Zefiro 23 (QM) and Zefiro 40 (DM) assuming both γ_{var} and γ_{fix} models.

Figure 15 show a comparison of the nozzle over-expansion condition (in terms of exit pressure over ambient pressure) for the SFTs of Zefiro 9 (QM2 and VT2), Zefiro 23 (QM) and Zefiro 40 (DM). Note that the flight units of the Z23 SRM are nominally identical to the QM SFT unit, aside from the nozzle expansion ratio that is reduced for the SFT because of the constraint derived from the nozzle operation at atmospheric pressure. Differently, the Zefiro 23 DM SFT unit is not nominally the same SRM. In fact, for the Zefiro 23 QM a redesign of the nozzle was considered with respect to DM, using a reduced nozzle throat area while keeping the same nozzle expansion ratio, that resulted in a higher pressure and lower burning time with respect to DM SFT. Hence, Zefiro 23 DM has been excluded from this analysis. Similarly, Zefiro 9 VT has been excluded from this analysis. In fact, for the Zefiro 9 VT, a different nozzle design was tested with respect to QM2 and VT2 units (that were nominally identical to the flight units, aside from the nozzle expansion ratio that was reduced for the SFT), using an increased nozzle throat area that resulted in a lower pressure and higher burning time. As shown in Fig. 15, due to sea level operations, all SFT Zefiro nozzles operate in an over-expanded condition. Flow separation always occur during the tail-off phase for all SFTs (although Zefiro 9 is also separated at the early times). Zefiro 40 DM over-expansion level (up to 0.6 non dimensional time) lies in between Zefiro 23 and Zefiro 9 values. In terms of nozzle expansion ratio reduction, Zefiro 9 is characterized by the largest variation (from the SFT nozzle with $\epsilon = 21.49$ to the FU nozzle with $\epsilon = 72.45$) while Zefiro 23 is characterized by the smallest variation (from the SFT nozzle with $\epsilon = 15$ to the FU nozzle with $\epsilon = 25$). Zefiro 40, that ranges from $\epsilon = 20.8$ (SFT DM motor) up to $\epsilon = 37$ (FU motor), lies in between Zefiro 23 and Zefiro 9 although it is much closer to Zefiro 23.

To assess the thrust efficiency increase from SFTs to flights, Fig. 16 shows the efficiency curves as a function of time of the QM SFT and the VV01 to VV06 flights for Zefiro 23 motor (a single color is used for all flights to clearly distinguish them from the SFTs). Results have been computed assuming both γ_{var} and γ_{fix} models. Figure 17 shows the analogous comparison between SFTs (QM2 and VT2) and flights (VV01 to VV06) for Zefiro 9 motor (a single color is used for all flights to clearly distinguish them from the SFTs). The comparison among flights and SFTs shows an increase of the thrust efficiency from SFT to flight for

both Zefiro 23 and Zefiro 9 motors. To assess such an increase, results are presented in terms of average thrust efficiency. Note that, for each motor configuration (either SFT or flight) the highest thrust efficiency is always obtained with γ_{fix} model while the lowest thrust efficiency is always obtained with γ_{var} model. A time-averaged value (based on total impulse) of thrust efficiency can be computed for each flight and SFT data for both γ_{fix} and γ_{var} thrust coefficient-time evolution curves. Then, the highest (obtained from γ_{fix} model), lowest (obtained from γ_{var} model), and average (from γ_{fix} and γ_{var} model) time-averaged thrust efficiencies are additionally averaged among all SFTs and all flights. Results are shown in Figs. 16 and 17 where the highest (i.e. maximum), lowest (i.e. minimum), and average time-averaged thrust efficiency values (averaged over all SFTs and flights) are indicated for both flights and SFTs results. The flight/SFT data comparison shows that the thrust efficiency increases from SFT to flight by $\approx 1\%$ for Zefiro 23 (see Fig. 16). Moreover such an increase is shown to depend only slightly on the "gamma model". The flight/SFT data comparison shows that the thrust efficiency increases from SFT to flight by $\approx 2\%$ for Zefiro 9 (see Fig. 17). As for Zefiro 23, also for Zefiro 9 this increase of thrust efficiency is shown to depend only slightly on the "gamma model".

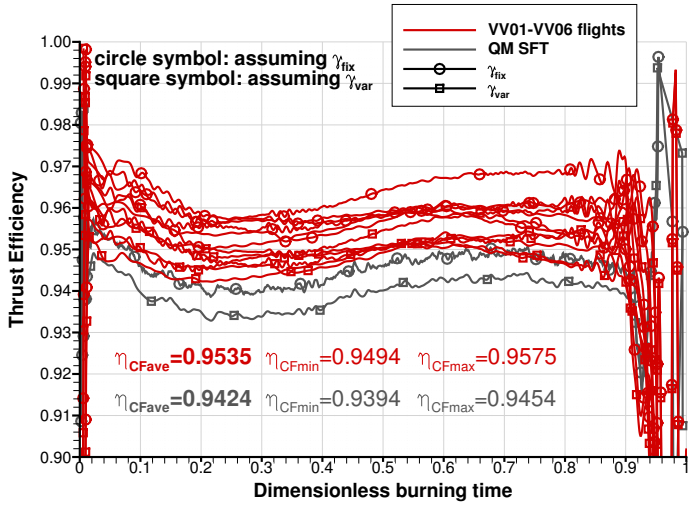

Figure 16. Zefiro 23 thrust efficiency curves for SFTs (QM) and flights (VV01 to VV06) assuming both γ_{var} and γ_{fix} models (the maximum, minimum, and average thrust efficiency values for both SFTs and flights are also indicated).

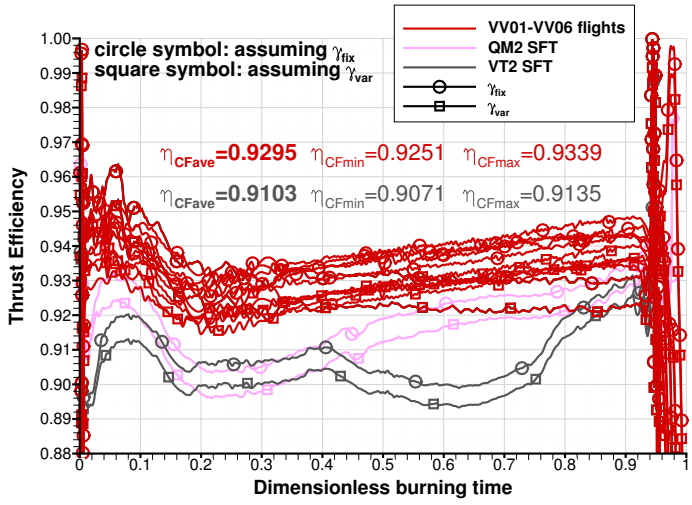

Figure 17. Zefiro 9 thrust efficiency curves for SFTs (QM) and flights (VV01 to VV06) assuming both γ_{var} and γ_{fix} models (the maximum, minimum, and average thrust efficiency values for both SFTs and flights are also indicated).

Based on Zefiro 23 expertise, two increments can be considered: the average one (corresponding to

+1.17% in thrust efficiency moving from SFT to flight) and the minimum one (corresponding to +0.42% in thrust efficiency moving from SFT to flight), which is deemed more conservative. Based on Zefiro 9 expertise, two increments can be considered: the average one (corresponding to +2.11% in thrust efficiency moving from SFT to flight) and the minimum one (corresponding to +1.27% in thrust efficiency moving from SFT to flight), which is deemed more conservative. Due to a non-negligible discrepancy that has been evidenced among predicted results and the reference results for the Zefiro 9 SFTs thrust efficiencies (with the reference results being significantly higher than the predicted results), the use of Zefiro 9 data to assess the thrust efficiency variation between flights and SFTs appears to be questionable. Hence, taking also into account the large similarity of Zefiro 40 nozzle with respect to Zefiro 23 nozzle and overall motor in general, predicted results based on Zefiro 23 thrust efficiency increase from SFT to flight appear more reliable. Moreover, the average thrust efficiency increase from SFT to flights appears to be the most reasonable choice.

In summary, a thrust efficiency increase from SFT to flights of +1.17% has been assessed based on Zefiro 23 flight data expertise and will be used for the performance extrapolation to flight unit performed in the following.

VII. Performance extrapolation to flight unit

In order to perform the extrapolation to the flight unit it is important to stress that, in terms of propellant formulation, some differences are always present in terms of additives and particles granulometry among the flight unit (FU) and demonstration (DM) and qualification (QM) motors, in order to obtain the desired propellant characteristics in terms of ballistic parameters and combustion. Hence, aside from a different nozzle expansion ratio (complete vs reduced) and a different operational condition (vacuum vs sea level), a burning time variation is also envisaged between the SFT motor and the FU motor because of the different burning rate (which is also slightly enhanced by a higher average propellant grain temperature of about 5 °C due to the different geographical location of the rocket testing range of Salto di Quirra, Italy, and of Europe's Spaceport, French Guyana). Such a burning time variation, not present in the SFT to FC analysis, does not allow to directly adopt the same thrust efficiency-time curve and the throat diameter-time curve from SFT to FU. Concerning the former curve, previous analyses have shown that the effect of assuming a time-variable thrust efficiency or a constant average value (based on total impulse) on the reconstructed thrust curve is minimal. Hence, the average thrust efficiency value reconstructed from the static firing test (that varies with the throat erosion law and the "gamma model") can be effectively adopted to perform the extrapolation to the flight unit, exactly as it is done for the combustion efficiency value (that is assumed as a constant value over time). As far as the throat erosion evolution is concerned, the use of a functional law such as the BPM, effectively bypass the problem of extrapolating the throat diameter-time curve. Hence, once the BPM functional law is selected (choosing the appropriate time delay), the corresponding values for the combustion efficiency, the average thrust efficiency (that also depends upon the "gamma model"), the scale factor, and the hump vs web curve are retrieved from the inverse approach. Those parameters can be effectively used in the direct approach to reconstruct the pressure-time and the thrust-time curves of the FU motor.

The direct approach relies on the same 0D quasi-steady model that is used for the inverse approach, whose results have been discussed in the previous part, with the substantial difference that the ballistic input and output parameters are inverted. Hence, the direct approach is able to provide the thrust and the pressure curve from the knowledge of the non-ideal parameters while the other input data remain the same of the inverse approach (the propellant burning rate characteristics and initial temperature, the propellant thermochemical characterization, the burning surface evolution vs web, the nozzle expansion ratio, the total propellant mass loaded, the igniter propellant mass, the thermal protection & liner ejected mass, the nozzle & igniter thermal protection ejected mass, and the alumina slag - if any - deposition mass).

Figure 18 shows the Zefiro 40 QM performance extrapolated to the Critical Design Review flight unit (nominal design) using the direct approach, both in terms of chamber pressure and vacuum thrust. Performance are extrapolated assuming BPM calibrated (with 3 s delay) with γ_{var} model and using a constant average value for the thrust coefficient. For the vacuum thrust extrapolation, a thrust efficiency increase from SFT to flights of +1.17% has been assumed basing on previous discussion. As shown in Fig. 18(a), the burning time is reduced while the maximum chamber pressure is increased passing from the SFTs to the FU. This effect is due to the different propellant burning rate parameters (both a and n) and the different initial propellant grain temperatures from SFTs to FU. It is worth noting that, although the effect of the

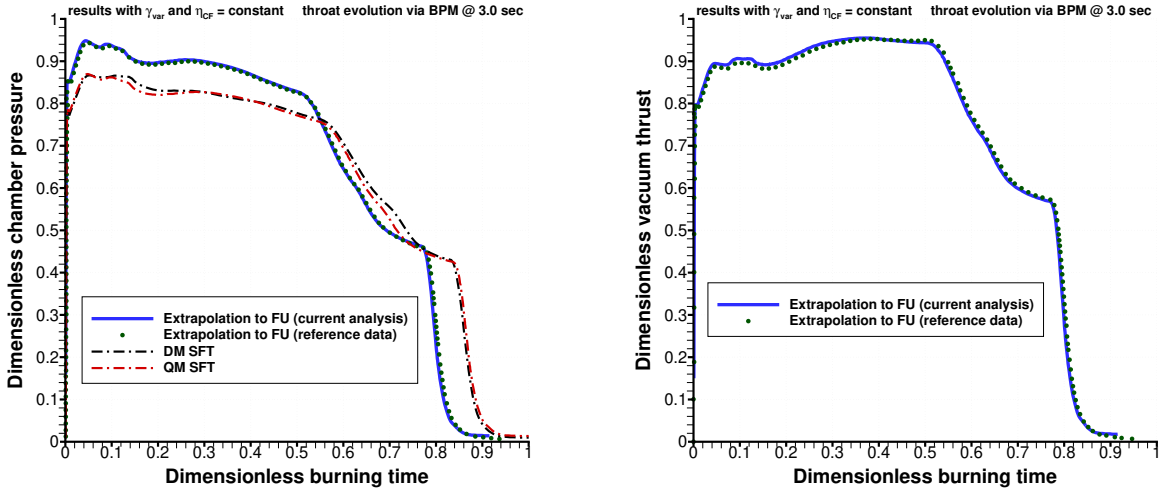

(a) Forward chamber pressure.

(b) Vacuum axial thrust.

Figure 18. Zefiro 40 QM performance extrapolated to the Critical Design Review flight unit (nominal design).

burning rate variation is significant in terms of pressure-time curve, it is substantially smaller in terms of specific impulse. In fact, the delivered vacuum I_{sp} varies from 293.4 s for the QM motor extrapolated in flight configuration to 293.6 s for the QM motor extrapolated to flight unit. Hence, there is a small variation of about 0.2 s passing from QM burning rate to FU burning rate. This is due to the fact that the chamber pressure is sufficiently high (also in the case of the lower burning rate of DM motor) so that the characteristic velocity increase with pressure is rather limited.

Table 5. Zefiro 40 performance and extrapolation to flight from SFTs expertise (values in brackets are obtained w/o assuming the thrust efficiency increase from SFT to flights based on Zefiro 23 expertise)

Motor	**DM** ($\epsilon = 20.8$)	**QM** ($\epsilon = 20.9$)
Sea/level specific impulse, s	245.7	243.3
Vacuum specific impulse, s	280.3	279.2
Flight Configuration (FC) specific impulse, s	295.0 [291.6]	293.4 [290.0]
Flight Unit (FU) specific impulse, s	295.2 [291.8]	293.6 [290.2]

In terms of thrust coefficient, as the thrust curves are computed in vacuum, there is no effect related to the chamber pressure increase from SFT to FU. Finally, in terms of final throat diameter, the FU prediction results in a final throat erosion on diameter that is 0.7 mm smaller with respect to the QM prediction. Hence, the different propellant burning rate characteristics and different initial temperature of FU with respect to QM also induce a variation of the final throat erosion. Fig. 18 also shows the reference extrapolation to FU performed by Avio (reference data). Results, that are obtained with different tools, are in close agreement with Avio predictions with a difference in the pressure integral of less than 0.1% and a difference in the thrust integral of less than 0.2%. Overall, results in terms of delivered specific impulse are indicated in Table 5. The delivered specific impulse of the FU motor ranges from 295.2 s if DM non-ideal parameters are assumed to 293.6 s if QM ones are assumed. The difference among the two predictions is 1.6 s and the average value is 294.4 s. The factor responsible for such a difference is mainly the difference in combustion efficiency (see Tab. 3). In fact, the BPM functional laws are almost identical (see Fig. 9(a)) and the thrust efficiencies are very similar (see Tab. 4) among DM and QM.

Aside from the combustion efficiency, another parameter that changes from DM and QM is the total hump curve (see Fig. 10(a)). The results in terms of QM extrapolation to FU using the total hump from QM and also from QM are shown in Fig. 19. Despite the different pressure and thrust curves, evidently affected

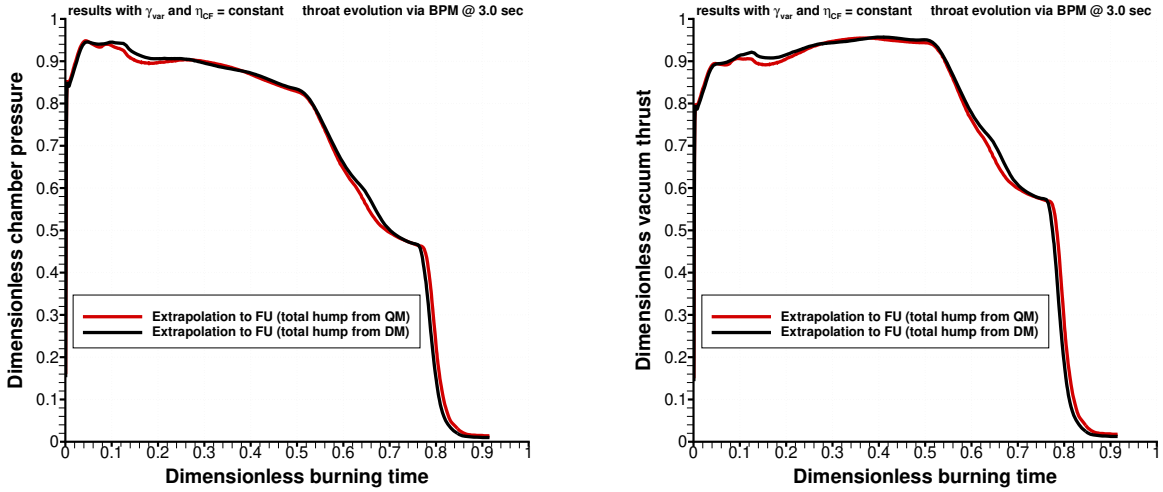

(a) Forward chamber pressure.

(b) Vacuum axial thrust.

Figure 19. Zefiro 40 QM performance extrapolated to the Critical Design Review flight unit (nominal design) using also the total hump curve from DM.

by the different total hump curve, the delivered vacuum specific impulse is practically unaffected (293.6 s).

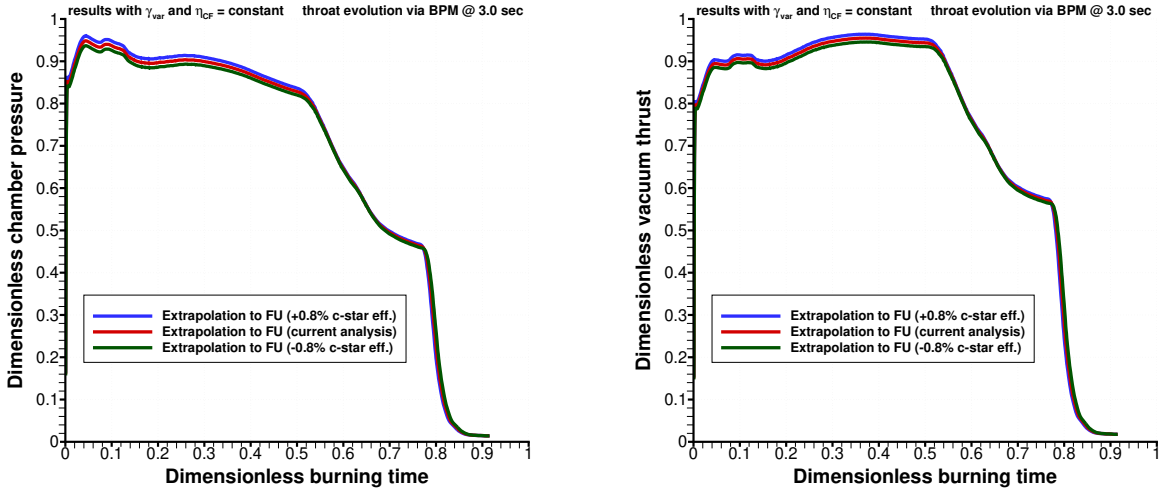

(a) Forward chamber pressure.

(b) Vacuum axial thrust.

Figure 20. Zefiro 40 QM performance extrapolated to the Critical Design Review flight unit (nominal design) assuming a prediction variability of the c-star efficiency of ± 0.8%.

To conclude the analysis, the effect of a variation in the combustion efficiency (assuming a prediction variability of $\pm 0.8\%$) on Zefiro 40 QM performance extrapolation to flight unit is shown in Fig. 20. The nominal predicted vacuum specific impulse of 293.6 s is increased to 295.3 s for a combustion efficiency increase of 0.8% and it is decreased to 291.8 s for a combustion efficiency decrease of 0.8%. Overall, the effect of $\pm 0.8\%$ on combustion efficiency results in roughly ± 1.7 s in terms of vacuum specific impulse. Finally, the effect of a variation in the throat eroded thickness (assuming a prediction variability of $\pm 35\%$) on Zefiro 40 QM performance extrapolation to flight unit is shown in Fig. 21. The nominal predicted vacuum specific impulse of 293.6 s is increased to 294.7 s for a throat erosion decrease of 35% and it is decreased to 292.5 s for a throat erosion increase of 35%. Overall, the effect of $\pm 35\%$ on nozzle throat erosion results in roughly ± 1.1 s in terms of vacuum specific impulse. It is worth noticing how the combustion efficiency

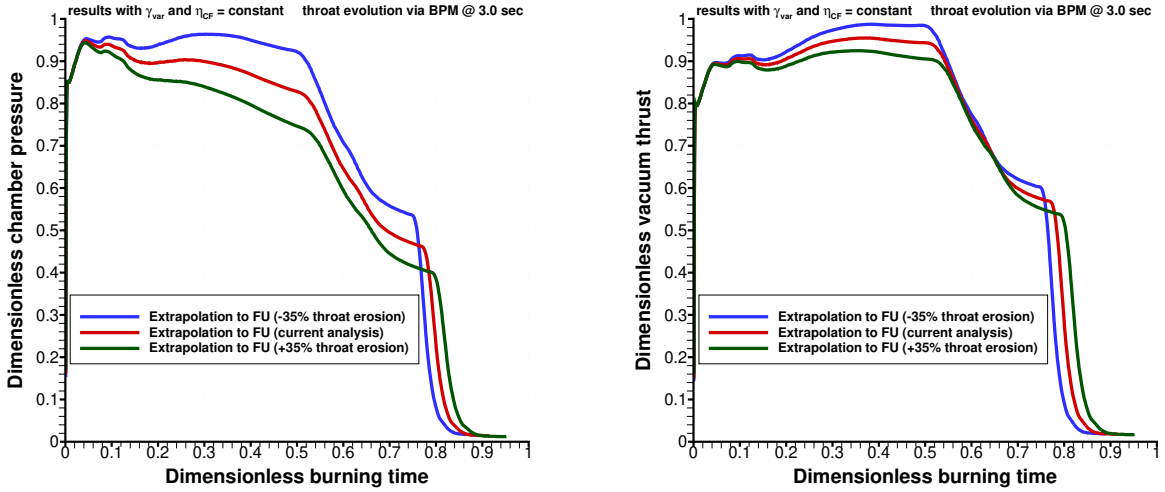

(a) Forward chamber pressure.

(b) Vacuum axial thrust.

Figure 21. Zefiro 40 QM performance extrapolated to the Critical Design Review flight unit (nominal design) assuming a prediction variability of the throat erosion of ±35%.

has a stronger effect on the vacuum specific impulse and a more limited effect on the performance curves (chamber pressure and axial thrust) while the nozzle throat erosion has a more limited effect on the vacuum specific impulse and a stronger effect on the performance curves.

VIII. Conclusions

A critical review and an independent assessment of the internal ballistics and performance reconstruction and extrapolation to flight for Zefiro 40 SRM DM and QM static firing tests has been performed, focusing on the motor quasi-steady state and tail-off phases. The SRM performance reconstruction model is based on a zero-dimensional quasi-steady modelling of the SRM internal ballistics, already used in the framework of previous activities with VEGA-IPT for the analysis of the VEGA motors SFTs and of the VEGA qualification and Verta flights. In the first part of the analysis, an assessment of the non-ideal parameters characterizing the actual SRM behavior has been carried out. In particular, the following parameters have been reconstructed for both SFTs: i) the hump curve and the scale factor; ii) the combustion efficiency; iii) the thrust efficiency curve; and iv) the nozzle throat area evolution. To deepen the performance assessment, a critical analysis of the effect of assuming different laws for the evolution of the throat area and of the effect of propellant thermochemical properties variation with combustion efficiency has been performed. In addition, a performance extrapolation of the DM and QM motor test to the actual flight configuration (vacuum condition and full nozzle expansion ratio) is performed.

In the second part of the analysis, a performance extrapolation to the flight unit SRM has been carried out in order to assess the thrust and pressure curves of the motor and the overall efficiency in terms of specific impulse as well as their variation due the prediction variability of the most important non-ideal parameters. Exploiting the SFT to flight expertise of Zefiro 23, a thrust coefficient increase from SFT to flight has been assessed and adopted for Zefiro 40 FU motor resulting in an increase of +1.17% in thrust efficiency moving from SFT to flight. Results of the extrapolation to flight unit showed that, although the effect of the burning rate variation from SFT to FU is significant in terms of pressure- and thrust-time curves, it is substantially negligible in terms of specific impulse. In fact, there is a variation of the vacuum specific impulse of only 0.2 s passing from SFT burning rate to FU burning rate. The FU motor specific impulse is assessed at 295.2 s when extrapolated from DM SFT and 293.6 s when extrapolated from QM SFT, under the assumption that the nozzle erosion behavior and the combustion efficiency do not change from SFT to flight. The average value of the specific impulse is 294.4 s and variability is ±0.8 s. Finally, an assessment of the scattering of nozzle throat erosion on motor specific impulse has been performed, resulting in ±1.1 s for a variation of ±35% on throat eroded thickness. An assessment of the scattering of motor combustion efficiency on

motor specific impulse has been also performed, resulting in ±1.7 s for a variation of ±0.8% on combustion efficiency.

IX. Acknowledgments

This work was supported and funded by the ESA-ESRIN/Contract No. 4000120618/17/I/AL "Technical Support Activities to Vega-C and Vega-E - Work Order 3". All the required motor data have been kindly granted by ESA ESRIN VEGA Integrated Project Team. The solid-fuel based Zefiro 40 motor, developed and manufactured by Avio in their Colleferro factory, will be the second stage motor of Europe's new-generation Vega-C launch vehicle. Avio is prime contractor for VEGA launcher and design authority for Zefiro 40 motor, while ESA oversees procurement and architecture of the overall launch system.

VEGA Programme has been managed by an Integrated Project Team that, under the responsibility of the European Space Agency (ESA), as a cooperative project with Member States within the ESA framework, involves also staff from the Italian (ASI) and French (CNES) Space Agencies.

References

[1]Daines, W. L. and Davis, D. K., "Status Review of Solid Propellant Rocket Motor Performance Prediction," AIAA Paper 1981–1377, 1981.

[2]George, D., "Recent Advances in Solid Rocket Motor Performance Prediction Capability," AIAA Paper 1981–0033, 1981.

[3]Langhenry, M. T. and Parks, J. M., "Reconstruction of Flight Specific Impulse for Solid Propellant Rocket Motors," AIAA Paper 1991–2428, 1991.

[4]Coats, D. E. and Dang, A. L., "Improvements to the Solid Performance Program (SPP'12) and a Review of Nozzle Performance Predictions," AIAA Paper 2014–3804, 2014.

[5]Cavallini, E., Favini, B., Di Giacinto, M., and Serraglia, F., "Analysis of VEGA Solid Stages Static Firing Tests towards the Maiden Flight," AIAA Paper 2012-4211, 2012.

[6]Bianchi, D., Favini, B., and Neri, A., "Performance Reconstruction of VEGA Solid Rocket Motors: VERTA Flights Experience," AIAA Paper 2018-4692, 2018.

[7]Bianchi, D., Grossi, M., Favini, B., Serraglia, F., Ierardo, N., Bucci, E., and Mucci, R., "Static Firing Ballistic Reconstruction Modelling and Performance Extrapolation to Flight in SRMs," AIAA Paper 2020-3925, 2020.

[8]Angelone, M., Mascanzoni, F., and Milana, C., "Technological and Programmatic Development of Zefiro 40 Solid Rocket Motor," AIAA Paper 2012-4213, 2012, doi: 10.2514/6.2012-4213.

[9]Di Trapani, C., Mataloni, A., Giliberti, F., Di Cosmo, A., N., P., and Milana, C., "Zefiro 40 Solid Rocket Motor Technological and programmatic development status," AIAA Paper 2014-3890, 2014, doi: 10.2514/6.2014-3890.

[10]Scoccimarro, D., Mucci, R., Marocco, R., Mataloni, A., Mancini, V., Genito, M., Milana, C., Neri, A., Bonnet, M., and Scaccia, A., "Zefiro 40 Solid Rocket Motor: From a Technological Demonstrator to Vega Evolution Flight Stage," AIAA Paper 2015-3877, 2015, doi: 10.2514/6.2015-3877.

[11]Bianchi, D., Nasuti, F., Onofri, M., and Martelli, E., "Thermochemical Erosion Analysis for Graphite/Carbon-Carbon Rocket Nozzles," *Journal of Propulsion and Power*, Vol. 27, No. 1, 2011, pp. 197–205, doi: 10.2514/1.47754.

[12]Cavallini, E., Bianchi, D., Favini, B., Di Giacinto, M., and Serraglia, F., "Internal Ballistics Modeling of High Performance SRMs with Coupled Nozzle Erosion Characterization," AIAA Paper 2011-5799, 2011.

[13]Bianchi, D. and Neri, A., "Numerical Simulation of Chemical Erosion in Vega Solid-Rocket-Motor Nozzles," *Journal of Propulsion and Power, in press*, 2018, doi: 10.2514/1.B36388.

[14]Cavallini, E., Favini, B., and Neri, A., "Effective Semi-Empirical Model of Nozzle Thermo-Chemical Erosion in Solid Rocket Motors," AIAA Paper 2017-4780, 2017.

[15]Kallmeyer, T. E. and Sayer, L. H., "Differences Between Actual and Predicted Pressure-Time Histories of Solid Rocket Motors," AIAA Paper 1982–1094, 1982.

[16]Gordon, S. and McBride, B. J., "Computer Program for Calculation of Complex Chemical Equilibrium Compositions and Applications," NASA RP 1311, 1994.

[17]Cavallini, E., Favini, B., Di Giacinto, M., and Serraglia, F., "SRM Internal Ballistic Numerical Simulation by SPINBALL Model," AIAA Paper 2009-5512, 2009.

[18]Cavallini, E., Favini, B., Di Giacinto, M., and Serraglia, F., "SRM Q1D unsteady Internal Ballistics Simulation using 3D Grain Burnback," Space Propulsion Conference, Propulsion for Space Transportation, 2010.

[19]Cavallini, E., *Modelling and Numerical Simulation of Solid Rocket Motors Internal Ballistics*, January 2010, PhD Dissertation, Università degli studi di Roma "La Sapienza", Rome, Italy.